ViewFormer: NeRF-free Neural Rendering from Few Images Using Transformers

Jonáš Kulhánek[1,2], Erik Derner[1,2], Torsten Sattler[1], and Robert Babuška[1,3]

[1] Czech Institute of Informatics, Robotics and Cybernetics,
Czech Technical University in Prague
{jonas.kulhanek,erik.derner,torsten.sattler}@cvut.cz
[2] Faculty of Electrical Engineering, Czech Technical University in Prague
[3] Cognitive Robotics Faculty of 3mE, Delft University of Technology
r.babuska@tudelft.nl

Abstract. Novel view synthesis is a long-standing problem. In this work, we consider a variant of the problem where we are given only a few context views sparsely covering a scene or an object. The goal is to predict novel viewpoints in the scene, which requires learning priors. The current state of the art is based on Neural Radiance Fields (NeRFs), and while achieving impressive results, the methods suffer from long training times as they require evaluating thousands of 3D point samples via a deep neural network for each image. We propose a 2D-only method that maps multiple context views and a query pose to a new image in a single pass of a neural network. Our model uses a two-stage architecture consisting of a codebook and a transformer model. The codebook is used to embed individual images into a smaller latent space, and the transformer solves the view synthesis task in this more compact space. To train our model efficiently, we introduce a novel *branching attention* mechanism that allows us to use the same model not only for neural rendering but also for camera pose estimation. Experimental results on real-world scenes show that our approach is competitive compared to NeRF-based methods while not reasoning in 3D, and it is faster to train.

Keywords: Novel view synthesis; Neural rendering; Localization

1 Introduction

Image-based novel view synthesis, *i.e.*, rendering a 3D scene from a novel viewpoint given a set of context views (images and camera poses), is a long-standing problem in computer graphics with applications ranging from robotics (*e.g.* planning to grasp objects) to augmented and virtual reality (*e.g.* interactive virtual meetings). Recently, the field has gained a lot of popularity thanks to Neural Radiance Field (NeRF) methods [42] that were successfully applied to the problem and outperformed prior approaches. Some methods use a proxy 3D model We distinguish between two variants of the view synthesis problem. The first variant renders a novel view from multiple context images taken from similar viewpoints [42,73]. Only a (very) sparse set of context images is provided in the

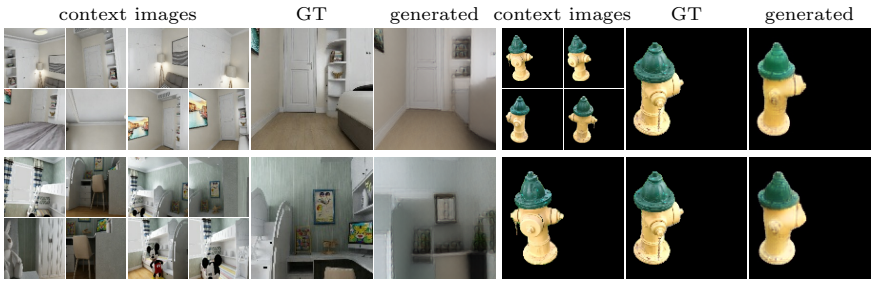

Fig. 1. Our novel view synthesis method renders images of previously unseen objects based on a few context images. It operates in 2D space without any 3D reasoning (as opposed to NeRF-based approaches [54,78]). The results are shown on the CO3D [54] and InteriorNet [33] datasets rendered for unseen scenes

second variant [54,78], *i.e.*, larger viewpoint variations and missing observations need to be handled. The latter task is much more difficult as it is necessary to learn suitable priors that can be used to predict unseen scene parts. This paper focuses on the second variant.

Recently, NeRF-based approaches were proposed to tackle this problem by learning priors for a class of objects and scenes [54,78]. These methods no longer learn a radiance field, but instead, they project image features from all context views into 3D. To render a new view, they shoot a ray through each pixel in the image plane into 3D, sample points along the rays, query the representation function at all sampled points, and aggregate the resulting features. While highly optimized NeRF approaches can be sped up such that they train in minutes on a single scene [45] (although requiring lots of images), this cannot be said about methods that generalize over classes of scenes and use only few context images to be able to represent a 3D scene. The radiance field values cannot be cached or otherwise optimized, because the methods generate them on-the-fly from the context views. In contrast, feed-forward networks can be highly efficient. However, explicitly encoding 3D geometric principles in them can be challenging. In our work, we thus pose the question: *Is reasoning in 3D necessary for high-quality novel view synthesis or can a purely image-based method achieve a competitive performance?*

Recently, Rombach *et al.* [57] successfully tackled single-view novel view synthesis, where the model was able to predict novel views without 3D reasoning. Inspired by these findings, we tackle the more complex problem of multi-view novel view synthesis. To answer the question, we propose a method with no 3D reasoning able to predict novel views using multiple context images in a forward pass of a neural network. We train our model on a large collection of diverse scenes to enable the model to learn 3D priors implicitly. Our approach is able to render a view in a novel scene, unseen at training time, three orders of magnitude faster than state-of-the-art (SoTA) NeRF-based approaches [54], while also being ten times faster to train. Furthermore, we are able to train a single model

to render multiple classes of scenes (see Fig. 1), whereas the SoTA NeRF-based approaches typically train per-class models [54].

Our model uses a two-stage architecture consisting of a Vector Quantized-Variational Autoencoder (VQ-VAE) codebook [47] and a transformer model. The codebook model is used to embed individual images into a smaller latent space. The transformer solves the novel view synthesis task in this latent space before the image is recovered via a decoder. This enables the codebook to focus on finer details in images while the transformer operates on shorter input sequences, reducing the quadratic memory complexity of its attention layer.

For training, we pass a sequence of views into the transformer and optimize it for all context sizes at the same time, effectively utilizing all images in the training batch, which is different from other methods [20, 21, 48, 51] that train only one query view. Unlike autoregressive models [21, 48, 51], we do not decode images token-by-token but all tokens are decoded at once which is both faster and mathematically exact (while autoregressive models rely on greedy strategies). Therefore, our approach can be considered a combination of autoregressive [49, 72] and masked [17] transformer models. With the standard attention mechanism, the complexity would be quadratic in the number of views, because we would have to stack different query views corresponding to different context sizes along the batch dimension. Therefore, we propose a novel attention mechanism called *branching attention* with constant overhead regardless of how many query views we optimize. Finally, our attention mechanism also allows us to optimize the same model for the camera pose estimation task – predicting the query image's camera pose given a set of context views. Since the camera pose estimation task can be considered an "inverse" of the novel view synthesis task [76], we consider the ability to perform both tasks via the same model to be an intriguing property. Even though the localization results are not yet competitive with state-of-the-art localization pipelines, we achieve a similar level of pose accuracy as comparable methods such as [1, 63].

In summary, this paper makes the following contributions: **1**) We propose an efficient novel view synthesis approach that does not use 3D reasoning. Our two-stage method consisting of a codebook model and a transformer is competitive with state-of-the-art NeRF-based approaches while being more efficient to train. Compared to similar methods that do not use 3D reasoning [14, 20, 69], our approach is not only evaluated on synthetic data but performs well on real-world scenes. **2**) Our transformer model is a combination of an autoregressive and a masked transformer. We propose a novel attention mechanism called *branching attention* that allows us optimize for multiple context sizes at once with a constant memory overhead. **3**) Thanks to the branching attention, our model can both render a novel view from a given pose and predict the pose for a given image. **4**) We publish the source code and the pre-trained models.[4]

[4] https://github.com/jkulhanek/viewformer

2 Related work

Novel view synthesis has a long history [11, 66]. Recently, deep learning techniques have been applied with great success, enabling higher realism and flexibility [15,24,40,55,56]. Some approaches use explicit reconstructed geometry to warp context images into the target view [15, 24, 55, 56, 68]. In our approach, we do not require any proxy geometry and only operate on 2D images.

Neural Radiance Fields (NeRF) methods [27, 37, 40, 40, 42, 53, 77] use neural networks to represent the continuous volumetric scene function. To render a view, for each pixel in the image plane, they project a ray into 3D space and query the radiance field in 3D points along each ray. The radiance field is trained for each scene separately. Some methods generalize to new scenes by conditioning the continuous volumetric function on the context images [58, 67], which allows them to utilize trained priors and render views from scenes on which the model was not trained, much like our approach. Other approaches remove the trainable continuous volumetric scene function altogether. Instead, they reproject the context image's features into the 3D space and apply the NeRF-based rendering pipeline on top of this representation [25, 54, 71, 73, 78]. Similarly to these methods, our approach also utilizes few context views (less than 20), and it also generalizes to unseen objects. However, we do not use the continuous volumetric function nor the reprojection into the 3D space. A different approach, IBRNet [73], learns to copy existing colors from context views, effectively interpolating the context views. Unlike ours, it thus cannot be applied to the settings where the context views are sparsely distributed around the object [25,54,71,78].

A different line of work directly maps 2D context images to the 2D query image using an end-to-end neural network [14, 20, 69]. GQN-based methods [14, 20, 69] apply a CNN to context images and camera poses and combine the resulting features. While some GQN methods [14, 20] do not use any 3D reasoning (same as our approach), Tobin *et al.* [69] uses an epipolar attention. We optimize our model on all context images and fully utilize the training sequences, whereas GQN methods optimize only the query views.

A recent work by Rombach *et al.* [57] proposed an approach for novel view synthesis without explicit 3D modeling. They used a codebook and a transformer model (same as we do) to map a single context view to a novel view from a different pose. Their approach is limited in its scope to mostly forward facing scenes where it is easier to render the novel view given a single context view and the poses have to align well. Their approach cannot be extended to more views due to the limit on the sequence size of the transformer model. However, in our approach, we focus on using multiple context views, which we tackle through using smaller latent space and utilizing the proposed branching attention. Furthermore, we can jointly train and use the same model for both the novel view synthesis and camera pose estimation. Also, our decoding is faster since we do not decode the output token-by-token, but the image is decoded at once.

Visual localization. There is an enormous body of work tackling the problem of localization, where the goal is to output the camera pose given the camera

image. *Structure-based* approaches use correspondences between 2D pixel positions and 3D scene coordinates for camera pose estimation [5,10,35,39,59,61,65]. Our method does not reason in 3D space, and the camera pose is instead predicted by the network. Simple *image retrieval* (IR) approaches store a database of all images with camera poses and for each query image they try to find the most similar images [8,9,16,26,62,80] and use them to estimate the pose of the query. IR methods can also be used to select relevant images for accurate pose estimation [3,26,59,80,81].

Pose regression methods train a convolutional neural network (CNN) to regress the camera pose of an input image. There are two categories: *absolute pose regression* (APR) methods [4,7,13,28,30,34,43,63] and *relative pose regression* (RPR) methods [1,18,32,34,41]. However, [62] showed that APR is often not (much) more accurate than IR. RPR methods do not train a CNN per scene or a set of scenes, but instead condition the CNN on a set of context views. While our approach performs relative pose regression, the main focus of our method is on the novel view synthesis. Some pose regression methods use novel view synthesis methods [13,43,44,46], however, they assume there is a method that generates images, whereas our method performs both the novel view synthesis and camera pose regression in a single model. *Iterative refinement* pose regression methods [60,76] start with an initial camera pose estimate and refine it by an iterative process, however, our approach generates the novel views and the camera pose estimates in a single forward pass.

3 Method

In this work, we tackle the problem of image-based novel view synthesis – given a set of *context* views, the algorithm has to generate the image it would most likely observe from a *query* camera pose. We focus on the case where the number of context views is small, and the views sparsely cover the 3D scene. Thus, the algorithm must hallucinate parts of the scene in a manner consistent with the context views. Therefore, it is necessary to learn a prior over a class of scenes (*e.g.*, all indoor environments) and use this prior for novel scenes. Besides rendering novel views, our model is also capable of performing camera pose estimation, *i.e.*, the "inverse" of the view synthesis problem: given a set of context views and a query image, the model outputs the camera pose from which the image was taken.

Our framework consists of two components: a codebook model and a transformer model. The codebook is used to map images to a smaller discrete latent space (*code space*), and back to the image space. In the *code space*, each image is represented by a sequence of *tokens*. For the novel view synthesis task, the transformer is given a set of context views in the code space and the query camera pose, and it generates an image in the *code space*. The codebook maps the image tokens back to the image space. See Fig. 2 for an overview. For the camera pose estimation task, the transformer is given the set of context views and the query image in the code space, and it generates the camera pose using a

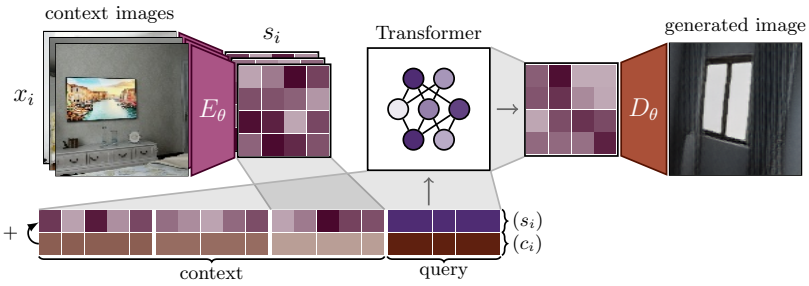

Fig. 2. Inference pipeline. The context images x_i are encoded by the codebook's encoder E_θ to the code representation s_i. We embed all tokens in s_i, and add the transformed camera pose c_i. The transformer generates the image tokens which are decoded by the codebook's decoder D_θ

regression head attached to the output of the transformer corresponding to the query image tokens.

Having the codebook and the transformer as separate components was inspired by recent work on image generation [21,51,57]. The main motivation is to decrease the transformer's space complexity which grows quadratically with the token sequence size. In our case, it also allows us to separate image generation and view synthesis, enabling us to train the transformer more efficiently in a simpler space.

Codebook model is a VQ-VAE [47,52], which is a variational autoencoder with a categorical distribution over the latent space. The model consists of two parts: the encoder E_θ and decoder D_θ. The encoder first reduces the dimension of the input image from 128×128 pixels to 8×8 tokens by several strided convolution layers. The convolutional part is followed by a quantization layer, which maps the resulting feature map to a discrete space. The quantization layer stores n_{lat} embedding vectors of the same dimension as the feature vectors returned by the convolutional part of the encoder. It encodes each point of the feature map by returning the index of the closest embedding vector. The output of the encoder at position (i, j) for image x is:

$$\arg\min_k \|(f_\theta^{(enc)}(x))_{i,j} - W_k^{(emb)}\|_2 \,, \tag{1}$$

where $W^{(emb)} \in \mathbb{R}^{n_{lat} \times d_{lat}}$ is the embedding matrix with rows W_k of length d_{lat} and $f_\theta^{(enc)}$ is the convolutional part of the encoder. The decoder then performs an inverse operation by first encoding the indices back to the embedding vectors by using $W^{(emb)}$ followed by several convolutional layers combined with upscaling to increase the spatial dimension back to the original image size.

Since the operation in Eq. (1) is not differentiable, we approximate the gradient with a straight-through estimator [2] and copy the gradients from the decoder input to the encoder output. The final loss for the codebook is a sum of three parts: the pixel-wise mean absolute error (MAE) between the input

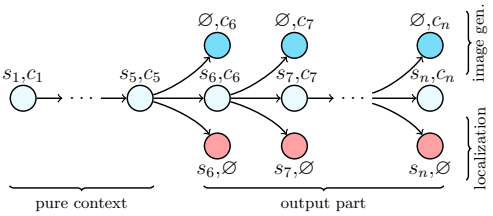

Fig. 3. In the **branching attention** mechanism, nodes represent parts of the processed sequence. Starting in any node and tracing the arrows backwards gives the sequence over which the attention is computed, *e.g.*, node $s_7, \varnothing$ attends to s_1, c_1, s_2, c_2, $\ldots$, $s_7, \varnothing$. Dark-colored nodes represent the type of output later used in the loss computation

image and the reconstructed image, the perceptual loss between the input and reconstructed image [21], and the commitment loss [47,52] which encourages the output of the encoder to stay close to the chosen embedding vector to prevent it from fluctuating too frequently from one vector to another:

$$\min_k \beta ||f_\theta^{(enc)}(x)_{i,j} - \mathrm{sg}(W_k^{(emb)})||_2^2 \,, \tag{2}$$

where sg is the stop-gradient operation [47]. We use the exponential moving average updates for the codebook [47]. More details about the codebook training are given in [47,52]. See the *supp. mat.* for the architecture details.

Transformer. We first describe the case of image generation and extend the approach to camera pose estimation later. We want to optimize the transformer for multiple context sizes and multiple query views in the batch at the same time. This has two benefits: it will allow the trained model to handle different context sizes, and the transformer will utilize the training batch fully (multiple images will be loss targets). Each training batch consists of a set of n views. Let $(x_i)_{i=1}^n$ be the sequence of images under a random ordering and $(c_i)_{i=1}^n$ be the sequence of the associated camera poses. Let us also define the sequence of images transformed by the encoder model E_θ parametrized by θ as $(s_i = E_\theta(x_i))_{i=1}^n$. Note that each s_i is itself a sequence of tokens. With this formulation, we want to generate the next image in the sequence given all the previous views, effectively optimizing all different context sizes at once. Therefore, we model the probability $p(s_i|s_{<i}, c_{\leq i})$. Note that we do not optimize the first $n_{\min}$ views, because they usually do not provide enough information for the task.

In practice, we need to replace the tokens corresponding to each query view with mask tokens to allow the transformer to decode them in a single forward pass. For the image generation task, the tokens of the last image in the sequence are replaced with special mask tokens λ, and for the localization task, the tokens of the last image do not include the camera pose (denoted as $\varnothing$). However, if we replaced the tokens in the training batch the next query image would not be able to perceive the original tokens, therefore, we have to process both the original tokens and masked ones. For i-th query image, we need the sequence of

$i-1$ context views ending with masked tokens at i-th position. We can represent the sequences in a tree where different ending branch off the shared trunk. This tree is visualized in Fig. 3. By following a leaf node back to the root of the tree, we recover the original sequence corresponding to the particular query view.

For localization, we train the model to output i-th camera pose c_i given $s_{\leq i}$ and $c_{<i}$. As for image generation, this leads to $n - n_{\min}$ sequences. We attach a regression head to the hidden representation of all tokens of the last image in the sequence. The query image tokens form the input, and we mask the camera poses by replacing the camera pose representation with a single trainable vector.

Branching attention. In this section, we introduce the *branching attention* which computes attention over the tree shown in Fig. 3, and allows us to optimize the transformer model for all context sizes and tasks very efficiently. Note that we have to forward all tree nodes through all layers of the transformer. Therefore, the memory and time complexity is proportional to the number of nodes in the tree and thus to the number of views and tasks.

The input to the branching attention is a sequence of triplets of keys, values and queries: $\left((K^{(i)}, Q^{(i)}, V^{(i)})\right)_{i=0}^{p}$ for $p = 2$, because we train the model on two tasks. Each element in the sequence corresponds to a single row in Fig. 3 and $i = 0$ is the middle row. All $K^{(i)}$, $Q^{(i)}$, $V^{(i)}$ have the shape $(nk^2) \times d_m$ where d_m is the dimensionality of the model and k is the size of the image in the latent space. The output of the branching attention is a sequence $\left(R^{(i)}\right)_{i=0}^{p}$. The case of $R^{(0)}$ is handled differently, because it corresponds to the trunk shared for all tasks and context sizes. Let us define an upper triangular matrix $M \in \mathbb{R}^{n \times n}$ as $(m)_{i,j} = \mathbb{1}_{i>j}$. We compute the causal block attention as:

$$R^{(0)} = \text{softmax}(Q^{(0)}(K^{(0)})^T - \infty(M \otimes \mathbf{1}^{k^2 \times k^2}))V^{(0)}\,, \tag{3}$$

where $\otimes$ is the Kronecker product, and $\mathbf{1}^{m \times n}$ is a matrix of ones. Eq. (3) is similar to normal masked attention [72] with the only difference in the causal mask. In this case, we allow the model to attend to all previous images and all other vectors from the same image. For $i > 0$ we can compute $R^{(i)}$ as follows:

$$D = Q^{(i)}(K^{(0)})^T - \infty((M + I) \otimes \mathbf{1}^{k^2 \times k^2}) \tag{4}$$

$$C = \begin{bmatrix} Q^{(i)}_{1:k^2}(K^{(i)}_{1:k^2})^T \\ \vdots \\ Q^{(i)}_{(n-1)\cdot k^2+1:n\cdot k^2}(K^{(i)}_{(n-1)\cdot k^2+1:n\cdot k^2})^T \end{bmatrix} \tag{5}$$

$$S = \text{softmax}([D, C]) \tag{6}$$

$$S' = S_{\cdot,1:n\cdot k^2}\,, S'' = S_{\cdot,n\cdot k^2+1:(n+1)\cdot k^2} \tag{7}$$

$$R^{(i)} = S'V^{(0)} + \begin{bmatrix} S''_{1:k^2}V^{(i)}_{1:k^2} \\ \vdots \\ S''_{n\cdot k^2+1:(n+1)\cdot k^2}V^{(i)}_{n\cdot k^2+1:(n+1)\cdot k^2} \end{bmatrix} \tag{8}$$

The matrix D represents the raw attention scores between ith queries and keys from all previous images. Matrix C contains the raw pairwise attention scores between ith queries and ith keys (the ending of each sequence). Then, the softmax is computed to normalize the attention scores, resulting in the attention matrix S, and the respective values are weighted by the computed scores. In particular, we need to redistribute the scores contained in the last k^2 columns of the attention matrix back to the associated ith values. The result $R^{(0)}$ corresponds to the nodes in the middle row in Fig. 3, whereas $R^{(i)}, i > 0$ are the other nodes.

Transformer input and training. To build the input for the transformer, we first embed all image tokens into trainable vector embeddings of length d_m. Before passing camera poses to the network, we express all camera poses relative to the first context camera pose in the sequence. We represent camera poses by concatenating the 3D position with the normalized orientation quaternion (a unit quaternion with a positive real part). Finally, we transform the camera poses with a trainable feed-forward neural network in order to increase the dimension to the same size as image token embeddings d_m in order to be able to sum them.

Similarly to [49], we also add the positional embeddings by summing the input sequence with a sequence of trainable vectors. However, our positional embeddings are shared for all images in the sequence, *i.e.*, ith token of every image will share the same positional embedding.

The output of the last transformer block is passed to an affine layer followed by a softmax layer, and it is trained using the cross-entropy loss to recover the last k^2 tokens $(s_{j,1}, \ldots, s_{j,k^2})$. For the localization task, the output is passed through a two-layer feed-forward neural network, and it is trained using the mean square error to match the ground-truth camera pose of the last k^2 tokens. Note that we compute the losses over position and orientation separately and add them together without weighing.[5] Since we attach the pose prediction head to the hidden representation of all tokens of the query image, we obtain multiple pose estimates. During inference, we simply average them.

4 Experiments

To answer the question whether 3D reasoning is really needed for novel view synthesis, we designed a series of experiments evaluating the proposed approach. First, we evaluate the codebook whose performance is the upper bound on what we can achieve with the full pipeline. We next compare our method to GQN-based methods [13,20,69] that also do not use continuous volumetric scene functions. We continue by evaluating our approach on other synthetic data. Then, we compare our approach to state-of-the-art NeRF-based approaches on a real-world dataset. Finally, we show our model's localization performance.

We evaluate our approach on both real and synthetic datasets: a) **Shepard-Metzler-7-Parts (SM7)** [20,64] is a synthetic dataset, where objects composed

[5] We tried dynamic weighting described in [29], but it performed worse.

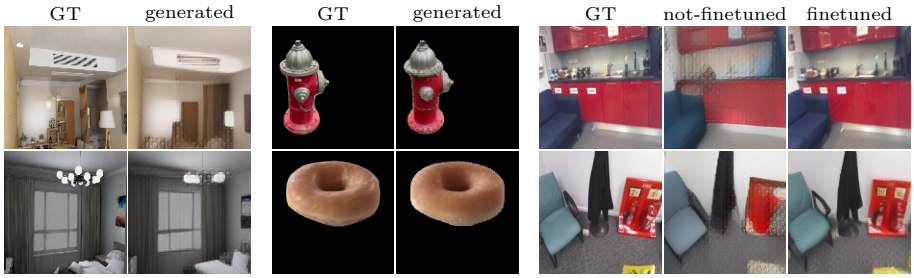

(a) InteriorNet [33] (b) CO3D [54] (c) 7-Scenes [22]

Fig. 4. Codebook evaluation on multiple datasets comparing the ground truth (**GT**) with the reconstructed image. For the InteriorNet dataset, we compare the model finetuned and not-finetuned on the 7-Scenes dataset.

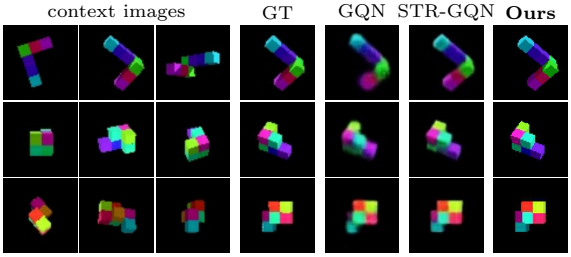

Fig. 5. Results on the SM7 dataset. We compare against GQN [20] and STR-GQN [14]

of 7 cubes of different colors are rotated in space. b) **ShapeNet** [12] is a synthetic dataset of simple objects. We use 128×128 pixel images rendered by [67] containing two categories: cars and chairs. c) **InteriorNet** [33] is a collection of interior environments designed by 1100 professional designers. We used the publicly available part of the dataset (20k scenes with 20 images each). While the dataset is synthetic, the renderings are similar to real-world environments. The first 600 environments serve as our test set. d) **Common Objects in 3D (CO3D)** [54] is a real-world dataset containing 1.5 million images showing almost 19k objects from 51 MS-COCO [36] categories (*e.g.*, apple, donut, vase, ...). The capture of the dataset was crowd-sourced. e) **7-Scenes** [22] is a real-world dataset depicting 7 indoor scenes as captured by a Kinect RGB-D camera. The dataset consists of 44 sequences of 500–1 000 frames each and it is a standard benchmark for visual localization [1, 7, 30, 32, 41].

Codebook evaluation. First, we evaluate the quality of our codebooks by measuring the quality of the images generated by the encoder-decoder architecture without the transformer. We trained codebooks of size 1024 using the same hyperparameters for all experiments using an architecture very similar to [21].

Fig. 6. Evaluation of our method on the InteriorNet dataset with the context size 19

The training took roughly 480 GPU-hours. A detailed description of the model and the hyperparameters is given in *supp. mat.* as well as in the published code.

Examples of reconstructed images are shown in Fig. 4. As can be seen, although losing some details and image sharpness, the codebooks can recover the overall shape well. The results show that using the codebook leads to good results, even though we use only 8×8 codes to represent an image. In some images there are noticeable artifacts. In our analysis we pinpointed the perceptual loss to be the cause, but removing the perceptual loss led to more blurry images. Further analysis of the codebooks is included in the *supp. mat.*

Full method evaluation. The transformer is trained using only the tokens generated by the codebook. Having verified that our codebooks work as intended, we evaluate our complete approach in the context of image synthesis. The architecture of our transformer model is based on GPT2 [49]. We give more details on the architecture, the motivation, and the hyperparameters in the *supp. mat.*

SM7 dataset was used to compare our approach to other methods that only operate in 2D [14, 20, 69]. Our method achieved the best mean absolute error (MAE) of **1.61**, followed by E-GQN [69] with 2.14, STR-GQN [13] with 3.11 and the original GQN [20] method with MAE 3.13. The results were averaged over 1000 scenes (context size was 3) and computed on images with size 64×64 pixels. Qualitative comparison is shown in Fig. 5.

InteriorNet dataset was used because of its large size and realistic appearance. We also use models pre-trained on InteriorNet in other experiments. Since each scene provides 20 images, we use 19 context views. Fig. 6 shows images generated by the model trained on both the localization and novel view synthesis.

ShapeNet evaluation. We fine-tuned the model pre-trained on the InteriorNet dataset on the ShapeNet dataset. We trained a single model for both categories (cars and chairs) using 3 context views. The training details and additional results are given in *supp. mat.* We show the qualitative comparison with PixelNeRF [78] in Fig. 7. PixelNeRF trained a different model for each category.

The results show that our method achieves good visual quality overall, especially on the cars dataset. However, the geometry is slightly distorted on the

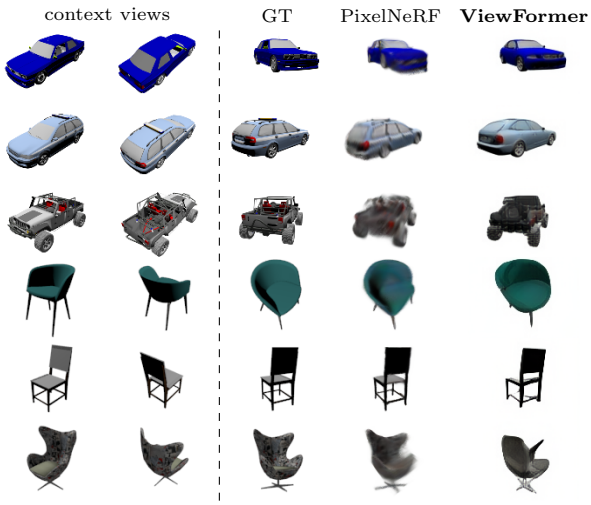

Fig. 7. ShapeNet qualitative comparison with PixelNeRF [78] using two context views

Table 1. Novel view synthesis results on the CO3D dataset [54] on all categories and 10 categories from [54]. We compare ViewFormer with and without localization ('no-loc') trained on all categories ('@ all cat.') and 10 selected categories ('@ 10 cat.'). We show the PSNR and LPIPS for seen and unseen scenes ('train' and 'test') and test PSNR with varying context size. The best value is **bold**; the second is underlined

			avg. test		avg. train		PSNR↑ @ # ctx. size				
EC	Method	3D	PSNR↑	LPIPS↓	PSNR↑	LPIPS↓	9	7	5	3	1
all categories	**ViewFormer @ all cat.**	✗	15.3	**0.23**	15.6	**0.22**	16.1	15.9	15.5	15.1	13.7
	ViewFormer no-loc @ all cat.	✗	15.4	**0.23**	15.8	**0.22**	16.2	16.0	15.6	15.2	13.8
	NerFormer [54]	✗	**15.7**	0.24	16.5	0.24	**16.7**	**16.4**	**16.1**	**15.5**	**13.9**
	SRN+WCE	✗	14.2	0.27	16.3	0.25	14.4	14.3	14.3	14.2	13.5
	SRN+WCE+γ	✗	13.7	0.28	**17.1**	0.25	14.0	13.8	13.9	13.7	13.2
	NeRF+WCE [25]	✗	11.6	0.27	12.6	0.27	11.9	11.8	11.8	11.6	10.8
10 categories	**ViewFormer @ 10 cat.**	✗	15.6	**0.25**	16.6	0.23	16.5	16.3	15.8	15.3	14.0
	ViewFormer no-loc @ 10 cat.	✗	15.6	**0.25**	17.1	**0.22**	16.5	16.2	15.8	15.3	14.0
	ViewFormer @ all cat.	✗	16.0	**0.25**	16.4	0.24	17.0	16.7	16.3	15.7	14.3
	ViewFormer no-loc @ all cat.	✗	16.1	**0.25**	16.6	0.23	17.0	16.8	16.3	15.8	14.3
	NerFormer [54]	✓	**17.6**	0.27	**17.9**	0.26	**18.9**	**18.6**	**18.1**	**17.1**	**15.1**
	SRN+WCE+γ	✓	14.4	0.27	17.6	0.24	14.6	14.5	14.6	14.5	13.9
	SRN+WCE	✓	14.6	0.27	16.6	0.26	14.9	14.8	14.8	14.6	13.9
	NeRF+WCE [25]	✓	13.8	0.27	14.3	0.27	12.6	14.5	14.4	14.2	13.8
	IPC+WCE	✓	13.5	0.37	14.1	0.36	13.8	13.8	13.7	13.6	12.6
	P3DMesh	✓	12.4	0.26	17.2	0.23	12.6	12.5	12.5	12.5	12.1
	NV+WCE	✓	11.6	0.35	12.3	0.34	11.7	11.6	11.6	11.6	11.3

chairs. Compared to PixelNeRF, it prefers to hallucinate a part of the scene instead of rendering a blurry image.

Common Objects in 3D. In order to show that we can transfer a model pre-trained on synthetic data to real-world scenes, we evaluate our method on the CO3D dataset [54]. We compare our approach with different NeRF-based methods using the results reported in [54]. Unfortunately, we were not able to achieve good performance with the PixelNeRF method [78] and we omit it from the comparison. While the baselines are trained separately per category, we train two transformer models: one on the 10 categories used for evaluation in [54] and one for all dataset categories. To this end, we fine-tune the model trained on the InteriorNet dataset. The context size is 9. Details on the training and hyperparameters are given in *supp. mat.*

The testing set of each category in the CO3D dataset is split into two subsets. The first set contains images of objects seen during training, but the images were not seen. This set is referred to as 'train'. The other subset, called 'test', contains unseen objects. We use the evaluation procedure provided by Reizenstein *et al.* [54]. It evaluates the model on 1 000 sequences from each category with context sizes 1, 3, ..., 9. The peak signal-to-noise ratio (PSNR) and the LPIPS distance [79] are reported. Note that the PSNR is calculated only on foreground pixels. For more details on the evaluation procedure and the details on the compared methods, please see [54].

Tab. 1 shows results of the evaluation on all CO3D categories and on the 10 categories used for evaluation in [54]. Our method is competitive even though it does not reason in 3D as other baselines, does not utilize explicit object masks, and even though we trained a single model for all categories while other baselines are trained per category. Note that on the whole dataset, the top-performing method, NerFormer [54], was trained for about 8400 GPU-hours while training our codebook took 480 GPU-hours and fine-tuning the transformer took 90 GPU-hours, giving a total of 570 GPU-hours.[6] Also note that rendering a single view takes 178 s for the NerFormer and only 93 ms for our approach.

The results shows that our model has a large capacity (it is able to learn all categories while the baselines are only trained on a single category), and it benefits from more training data as can be seen when comparing models trained on 10 and all categories. Also, we observe that models evaluated on 10 categories have higher performance than models evaluated on all categories, suggesting that the categories selected by the authors of the dataset are easier to learn or of higher quality. All our models outperform all baselines in terms of LPIPS, which indicates that the images can look more realistic at the cost of possibly not matching the correct viewpoint exactly.

Fig. 1 and 8 show qualitative results for our method. Our approach is able to generalize well to unseen object instances, even though it tends to lose some details. To answer the original question if 3D reasoning is needed for novel view synthesis, based on our results, we claim that even without 3D reasoning, we are able to achieve similar results, especially when the data are noisy, as in the case of a real-world dataset.

[6] Training the transformer on InteriorNet took 280 GPU-hours.

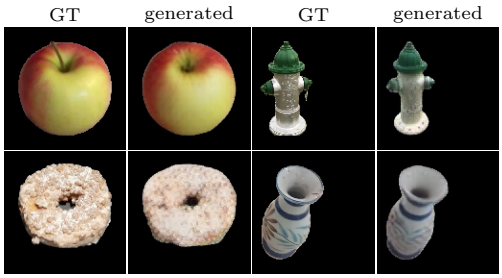

Fig. 8. Evaluation of our method on the CO3D dataset [54] with the context size 9

Evaluating localization accuracy on 7-Scenes. We compare the localization part of our approach to methods from the literature on the 7-Scenes dataset [22]. Due to space constraints, here we only summarize the results of the comparisons. Detailed results can be found in the *supp. mat.*

Our approach performs similarly to existing absolute pose and relative pose regression techniques that also use only a single forward pass in a network [1, 7, 30, 63], but worse than iterative approaches such as [18] or methods that use more densely spaced synthetic views as additional input data [43]. Note that all these approaches, which do not use 3D scene geometry for pose estimation, are less accurate than state-of-the-art methods based on 2D-3D correspondences [6, 59, 61]. Overall, the results show that our approach achieves a similar level of pose accuracy as comparable methods. Furthermore, our approach is able to perform both localization and novel view synthesis in simple forward pass, while other methods can only be used for localization.

5 Conclusions & future work

This paper presentes a two-stage approach to novel view synthesis from a few sparsely distributed context images. We train it on classes of similar 3D scenes to be able to generalize to a novel scene with only a handful of images as opposed to NeRFs and similar methods that are trained per scene. The model consists of a VQ-VAE codebook [47] and a transformer model. In order to efficiently train the transformer, we propose a novel branching attention module. Our approach, ViewFormer, can render a view from a previously unseen scene in 93 ms without any 3D reasoning and we train a single model to render multiple categories of objects, whereas state-of-the-art NeRF-based approaches train per-category models [54]. We show that our method is competitive with state-of-the-art NeRF-based approaches especially on real-world data, even though it does not use any explicit 3D reasoning. This is an intriguing result because it implies that either current NeRF-based methods are not utilizing the 3D priors effectively or that a 2D-only model is able to learn it on its own without any 3D supervision. Compared to other 2D-only methods, we achieve state-of-the-art performance.

One limitation of our approach is the large amount of data needed to learn a prior over a class of scenes, which we tackle through pre-training on a large synthetic dataset. Also, we need to fine-tune both the codebook and the transformer to achieve high-quality results in new scenarios, which could be resolved by utilizing a larger codebook trained on large image datasets. Using more tokens to represent images should increase the rendering quality and pose accuracy. We also want to experiment with a simpler architecture, where we will input the image pixels directly into the transformer instead of using the codebook, and evaluate our approach on larger scenes possibly of outdoor environments.

6 Acknowledgements

This work was supported by the European Regional Development Fund under projects Robotics for Industry 4.0 (reg. no. CZ.02.1.01/0.0/0.0/15_003/0000470) and IMPACT (reg. no. CZ.02.1.01/0.0/0.0/15_003/0000468), the EU Horizon 2020 project RICAIP (grant agreement No 857306), the Grant Agency of the Czech Technical University in Prague (grant no. SGS22/112/OHK3/2T/13), and the Ministry of Education, Youth and Sports of the Czech Republic through the e-INFRA CZ (ID:90140).

References

1. Balntas, V., Li, S., Prisacariu, V.: RelocNet: Continuous metric learning relocalisation using neural nets. In: Proceedings of the European Conference on Computer Vision (ECCV). pp. 751–767 (2018) 3, 5, 10, 14, 25, 27
2. Bengio, Y., Léonard, N., Courville, A.: Estimating or propagating gradients through stochastic neurons for conditional computation. arXiv preprint arXiv:1308.3432 (2013) 6
3. Bhayani, S., Sattler, T., Barath, D., Beliansky, P., Heikkilä, J., Kukelova, Z.: Calibrated and partially calibrated semi-generalized homographies. In: Proceedings of the IEEE/CVF International Conference on Computer Vision (ICCV) (2021) 5
4. Blanton, H., Greenwell, C., Workman, S., Jacobs, N.: Extending absolute pose regression to multiple scenes. In: Proceedings of the IEEE/CVF Conference on Computer Vision and Pattern Recognition Workshops. pp. 38–39 (2020) 5
5. Brachmann, E., Rother, C.: Visual camera re-localization from RGB and RGB-D images using DSAC. IEEE Transactions on Pattern Analysis and Machine Intelligence pp. 1–1 (2021). https://doi.org/10.1109/TPAMI.2021.3070754 5, 27
6. Brachmann, E., Rother, C.: Visual camera re-localization from RGB and RGB-D images using DSAC. IEEE Transactions on Pattern Analysis and Machine Intelligence (2021) 14, 25
7. Brahmbhatt, S., Gu, J., Kim, K., Hays, J., Kautz, J.: Geometry-aware learning of maps for camera localization. In: Proceedings of the IEEE Conference on Computer Vision and Pattern Recognition. pp. 2616–2625 (2018) 5, 10, 14, 25, 27
8. Camposeco, F., Cohen, A., Pollefeys, M., Sattler, T.: Hybrid camera pose estimation. In: Proceedings of the IEEE Conference on Computer Vision and Pattern Recognition. pp. 136–144 (2018) 5

9. Cao, S., Snavely, N.: Graph-based discriminative learning for location recognition. In: Proceedings of the IEEE Conference on Computer Vision and Pattern Recognition. pp. 700–707 (2013) 5
10. Cavallari, T., Golodetz, S., Lord, N.A., Valentin, J., Prisacariu, V.A., Di Stefano, L., Torr, P.H.S.: Real-time RGB-D camera pose estimation in novel scenes using a relocalisation cascade. TPAMI (2019) 5
11. Chan, S., Shum, H.Y., Ng, K.T.: Image-based rendering and synthesis. IEEE Signal Processing Magazine **24**(6), 22–33 (2007) 4
12. Chang, A.X., Funkhouser, T., Guibas, L., Hanrahan, P., Huang, Q., Li, Z., Savarese, S., Savva, M., Song, S., Su, H., et al.: ShapeNet: An information-rich 3D model repository. arXiv preprint arXiv:1512.03012 (2015) 10
13. Chen, S., Wang, Z., Prisacariu, V.: Direct-posenet: Absolute pose regression with photometric consistency. arXiv preprint arXiv:2104.04073 (2021) 5, 9, 11, 33
14. Chen, W.C., Hu, M.C., Chen, C.S.: STR-GQN: Scene representation and rendering for unknown cameras based on spatial transformation routing. In: Proceedings of the IEEE/CVF International Conference on Computer Vision. pp. 5966–5975 (2021) 3, 4, 10, 11, 30, 33
15. Choi, I., Gallo, O., Troccoli, A., Kim, M.H., Kautz, J.: Extreme view synthesis. In: Proceedings of the IEEE/CVF International Conference on Computer Vision. pp. 7781–7790 (2019) 4
16. Derner, E., Gomez, C., Hernandez, A.C., Barber, R., Babuška, R.: Change detection using weighted features for image-based localization. Robotics and Autonomous Systems **135**, 103676 (2021) 5
17. Devlin, J., Chang, M.W., Lee, K., Toutanova, K.: BERT: Pre-training of deep bidirectional transformers for language understanding. In: Proceedings of the 2019 Conference of the North American Chapter of the Association for Computational Linguistics: Human Language Technologies, Volume 1 (Long and Short Papers). pp. 4171–4186. Association for Computational Linguistics, Minneapolis, Minnesota (Jun 2019). https://doi.org/10.18653/v1/N19-1423, https://aclanthology.org/N19-1423 3, 28
18. Ding, M., Wang, Z., Sun, J., Shi, J., Luo, P.: CamNet: Coarse-to-fine retrieval for camera re-localization. In: Proceedings of the IEEE/CVF International Conference on Computer Vision. pp. 2871–2880 (2019) 5, 14, 25, 27
19. Engilberge, M., Collins, E., Susstrunk, S.: Color representation in deep neural networks. In: Proceedings of the IEEE International Conference on Image Processing. pp. 2786–2790 (2017) 22
20. Eslami, S.A., Rezende, D.J., Besse, F., Viola, F., Morcos, A.S., Garnelo, M., Ruderman, A., Rusu, A.A., Danihelka, I., Gregor, K., et al.: Neural scene representation and rendering. Science **360**(6394), 1204–1210 (2018) 3, 4, 9, 10, 11, 30, 33, 34, 35
21. Esser, P., Rombach, R., Ommer, B.: Taming transformers for high-resolution image synthesis. In: Proceedings of the IEEE/CVF Conference on Computer Vision and Pattern Recognition. pp. 12873–12883 (2021) 3, 6, 7, 10, 28, 34, 36
22. Glocker, B., Izadi, S., Shotton, J., Criminisi, A.: Real-time RGB-D camera relocalization. In: 2013 IEEE International Symposium on Mixed and Augmented Reality (ISMAR). pp. 173–179. IEEE (2013) 10, 14, 21, 25, 26, 34
23. He, K., Zhang, X., Ren, S., Sun, J.: Deep residual learning for image recognition. In: Proceedings of the IEEE conference on computer vision and pattern recognition. pp. 770–778 (2016) 36
24. Hedman, P., Philip, J., Price, T., Frahm, J.M., Drettakis, G., Brostow, G.: Deep blending for free-viewpoint image-based rendering. ACM Transactions on Graphics (TOG) **37**(6), 1–15 (2018) 4

25. Henzler, P., Reizenstein, J., Labatut, P., Shapovalov, R., Ritschel, T., Vedaldi, A., Novotny, D.: Unsupervised learning of 3D object categories from videos in the wild. In: Proceedings of the IEEE/CVF Conference on Computer Vision and Pattern Recognition. pp. 4700–4709 (2021) 4, 12
26. Irschara, A., Zach, C., Frahm, J.M., Bischof, H.: From structure-from-motion point clouds to fast location recognition. In: 2009 IEEE Conference on Computer Vision and Pattern Recognition. pp. 2599–2606. IEEE (2009) 5
27. Jain, A., Tancik, M., Abbeel, P.: Putting nerf on a diet: Semantically consistent few-shot view synthesis. In: Proceedings of the IEEE/CVF International Conference on Computer Vision. pp. 5885–5894 (2021) 4
28. Kendall, A., Cipolla, R.: Modelling uncertainty in deep learning for camera relocalization. In: 2016 IEEE International Conference on Robotics and Automation (ICRA). pp. 4762–4769. IEEE (2016) 5
29. Kendall, A., Cipolla, R.: Geometric loss functions for camera pose regression with deep learning. In: Proceedings of the IEEE Conference on Computer Vision and Pattern Recognition. pp. 5974–5983 (2017) 9
30. Kendall, A., Grimes, M., Cipolla, R.: PoseNet: A convolutional network for real-time 6-DOF camera relocalization. In: Proceedings of the IEEE International Conference on Computer Vision. pp. 2938–2946 (2015) 5, 10, 14, 25, 27
31. Kingma, D.P., Ba, J.: Adam: A method for stochastic optimization. In: ICLR (Poster) (2015) 34
32. Laskar, Z., Melekhov, I., Kalia, S., Kannala, J.: Camera relocalization by computing pairwise relative poses using convolutional neural network. In: Proceedings of the IEEE International Conference on Computer Vision Workshops. pp. 929–938 (2017) 5, 10
33. Li, W., Saeedi, S., McCormac, J., Clark, R., Tzoumanikas, D., Ye, Q., Huang, Y., Tang, R., Leutenegger, S.: InteriorNet: Mega-scale multi-sensor photo-realistic indoor scenes dataset. In: British Machine Vision Conference (BMVC) (2018) 2, 10, 21, 22, 27, 29, 30, 34
34. Li, X., Ling, H.: TransCamP: Graph transformer for 6-DoF camera pose estimation. ArXiv **abs/2105.14065** (2021) 5
35. Li, Y., Snavely, N., Huttenlocher, D.P., Fua, P.: Worldwide Pose Estimation Using 3D Point Clouds. In: ECCV (2012) 5
36. Lin, T.Y., Maire, M., Belongie, S., Hays, J., Perona, P., Ramanan, D., Dollár, P., Zitnick, C.L.: Microsoft COCO: Common objects in context. In: European Conference on Computer Vision. pp. 740–755. Springer (2014) 10
37. Liu, L., Gu, J., Zaw Lin, K., Chua, T.S., Theobalt, C.: Neural sparse voxel fields. Advances in Neural Information Processing Systems **33** (2020) 4
38. Loshchilov, I., Hutter, F.: Decoupled weight decay regularization. In: International Conference on Learning Representations (2018) 35
39. Lynen, S., Zeisl, B., Aiger, D., Bosse, M., Hesch, J., Pollefeys, M., Siegwart, R., Sattler, T.: Large-scale, real-time visual–inertial localization revisited. The International Journal of Robotics Research **39**(9), 1061–1084 (2020) 5
40. Martin-Brualla, R., Radwan, N., Sajjadi, M.S., Barron, J.T., Dosovitskiy, A., Duckworth, D.: NeRF in the wild: Neural radiance fields for unconstrained photo collections. In: Proceedings of the IEEE Conference on Computer Vision and Pattern Recognition. pp. 7210–7219 (2021) 4
41. Melekhov, I., Ylioinas, J., Kannala, J., Rahtu, E.: Relative camera pose estimation using convolutional neural networks. In: International Conference on Advanced Concepts for Intelligent Vision Systems. pp. 675–687. Springer (2017) 5, 10

42. Mildenhall, B., Srinivasan, P.P., Tancik, M., Barron, J.T., Ramamoorthi, R., Ng, R.: NeRF: Representing scenes as neural radiance fields for view synthesis. In: European Conference on Computer Vision. pp. 405–421. Springer (2020) 1, 4
43. Moreau, A., Piasco, N., Tsishkou, D., Stanciulescu, B., de La Fortelle, A.: LENS: Localization enhanced by NeRF synthesis. In: 5th Annual Conference on Robot Learning (2021) 5, 14, 25, 27
44. Mueller, M.S., Sattler, T., Pollefeys, M., Jutzi, B.: Image-to-image translation for enhanced feature matching, image retrieval and visual localization. ISPRS Annals of the Photogrammetry, Remote Sensing and Spatial Information Sciences **4**, 111–119 (2019) 5
45. Müller, T., Evans, A., Schied, C., Keller, A.: Instant neural graphics primitives with a multiresolution hash encoding. arXiv preprint arXiv:2201.05989 (2022) 2
46. Ng, T., Lopez-Rodriguez, A., Balntas, V., Mikolajczyk, K.: Reassessing the Limitations of CNN Methods for Camera Pose Regression. arXiv:2108.07260 (2021) 5
47. van den Oord, A., Vinyals, O., kavukcuoglu, k.: Neural discrete representation learning. In: Guyon, I., Luxburg, U.V., Bengio, S., Wallach, H., Fergus, R., Vishwanathan, S., Garnett, R. (eds.) Advances in Neural Information Processing Systems. vol. 30. Curran Associates, Inc. (2017), https://proceedings.neurips.cc/paper/2017/file/7a98af17e63a0ac09ce2e96d03992fbc-Paper.pdf 3, 6, 7, 14
48. Parmar, N., Vaswani, A., Uszkoreit, J., Kaiser, L., Shazeer, N., Ku, A., Tran, D.: Image transformer. In: International Conference on Machine Learning. pp. 4055–4064. PMLR (2018) 3, 28
49. Radford, A., Wu, J., Child, R., Luan, D., Amodei, D., Sutskever, I.: Language models are unsupervised multitask learners (2019) 3, 9, 11, 28, 35
50. Ramachandran, P., Zoph, B., Le, Q.V.: Searching for activation functions. arXiv preprint arXiv:1710.05941 (2017) 36
51. Ramesh, A., Pavlov, M., Goh, G., Gray, S., Voss, C., Radford, A., Chen, M., Sutskever, I.: Zero-shot text-to-image generation. arXiv preprint arXiv:2102.12092 (2021) 3, 6, 28, 34, 36
52. Razavi, A., van den Oord, A., Vinyals, O.: Generating diverse high-fidelity images with vq-vae-2. In: Wallach, H., Larochelle, H., Beygelzimer, A., d'Alché-Buc, F., Fox, E., Garnett, R. (eds.) Advances in Neural Information Processing Systems. vol. 32. Curran Associates, Inc. (2019) 6, 7
53. Reiser, C., Peng, S., Liao, Y., Geiger, A.: KiloNeRF: Speeding up neural radiance fields with thousands of tiny mlps. arXiv preprint arXiv:2103.13744 (2021) 4
54. Reizenstein, J., Shapovalov, R., Henzler, P., Sbordone, L., Labatut, P., Novotny, D.: Common objects in 3D: Large-scale learning and evaluation of real-life 3D category reconstruction. In: Proceedings of the IEEE/CVF International Conference on Computer Vision. pp. 10901–10911 (2021) 2, 3, 4, 10, 12, 13, 14, 21, 22, 23, 34, 35
55. Riegler, G., Koltun, V.: Free view synthesis. In: European Conference on Computer Vision. pp. 623–640. Springer (2020) 4
56. Riegler, G., Koltun, V.: Stable view synthesis. In: Proceedings of the IEEE/CVF Conference on Computer Vision and Pattern Recognition. pp. 12216–12225 (2021) 4
57. Rombach, R., Esser, P., Ommer, B.: Geometry-free view synthesis: Transformers and no 3d priors. In: Proceedings of the IEEE/CVF International Conference on Computer Vision. pp. 14356–14366 (2021) 2, 4, 6

58. Saito, S., Huang, Z., Natsume, R., Morishima, S., Kanazawa, A., Li, H.: PIFu: Pixel-aligned implicit function for high-resolution clothed human digitization. In: Proceedings of the IEEE/CVF International Conference on Computer Vision. pp. 2304–2314 (2019) 4
59. Sarlin, P.E., Cadena, C., Siegwart, R., Dymczyk, M.: From coarse to fine: Robust hierarchical localization at large scale. In: CVPR (2019) 5, 14, 25, 27
60. Sarlin, P.E., Unagar, A., Larsson, M., Germain, H., Toft, C., Larsson, V., Pollefeys, M., Lepetit, V., Hammarstrand, L., Kahl, F., et al.: Back to the feature: Learning robust camera localization from pixels to pose. In: Proceedings of the IEEE/CVF Conference on Computer Vision and Pattern Recognition. pp. 3247–3257 (2021) 5
61. Sattler, T., Leibe, B., Kobbelt, L.: Efficient & effective prioritized matching for large-scale image-based localization. IEEE Transactions on Pattern Analysis and Machine Intelligence **39**(9), 1744–1756 (2016) 5, 14, 25, 27
62. Sattler, T., Zhou, Q., Pollefeys, M., Leal-Taixe, L.: Understanding the limitations of CNN-based absolute camera pose regression. In: Proceedings of the IEEE/CVF Conference On computer Vision and Pattern Recognition. pp. 3302–3312 (2019) 5, 25, 27
63. Shavit, Y., Ferens, R., Keller, Y.: Learning multi-scene absolute pose regression with transformers. arXiv preprint arXiv:2103.11468 (2021) 3, 5, 14, 25, 27
64. Shepard, R.N., Metzler, J.: Mental rotation of three-dimensional objects. Science **171**(3972), 701–703 (1971) 9, 30, 34, 35
65. Shotton, J., Glocker, B., Zach, C., Izadi, S., Criminisi, A., Fitzgibbon, A.: Scene Coordinate Regression Forests for Camera Relocalization in RGB-D Images. In: CVPR (2013) 5
66. Shum, H., Kang, S.B.: Review of image-based rendering techniques. In: Visual Communications and Image Processing 2000. vol. 4067, pp. 2–13. International Society for Optics and Photonics (2000) 4
67. Sitzmann, V., Zollhöfer, M., Wetzstein, G.: Scene representation networks: Continuous 3D-structure-aware neural scene representations. arXiv preprint arXiv:1906.01618 (2019) 4, 10, 29, 30
68. Thies, J., Zollhöfer, M., Theobalt, C., Stamminger, M., Nießner, M.: Image-guided neural object rendering. In: 8th International Conference on Learning Representations. OpenReview. net (2020) 4
69. Tobin, J., Zaremba, W., Abbeel, P.: Geometry-aware neural rendering. Advances in Neural Information Processing Systems **32**, 11559–11569 (2019) 3, 4, 9, 11, 30, 33
70. Torii, A., Arandjelovic, R., Sivic, J., Okutomi, M., Pajdla, T.: 24/7 place recognition by view synthesis. In: Proceedings of the IEEE Conference on Computer Vision and Pattern Recognition. pp. 1808–1817 (2015) 25
71. Trevithick, A., Yang, B.: GRF: Learning a general radiance field for 3d representation and rendering. In: Proceedings of the IEEE/CVF International Conference on Computer Vision. pp. 15182–15192 (2021) 4
72. Vaswani, A., Shazeer, N., Parmar, N., Uszkoreit, J., Jones, L., Gomez, A.N., Kaiser, Ł., Polosukhin, I.: Attention is all you need. In: Advances in neural information processing systems. pp. 5998–6008 (2017) 3, 8, 28
73. Wang, Q., Wang, Z., Genova, K., Srinivasan, P.P., Zhou, H., Barron, J.T., Martin-Brualla, R., Snavely, N., Funkhouser, T.: IBRNET: Learning multi-view image-based rendering. In: Proceedings of the IEEE/CVF Conference on Computer Vision and Pattern Recognition. pp. 4690–4699 (2021) 1, 4
74. Wang, Z., Bovik, A.C.: Mean squared error: Love it or leave it? a new look at signal fidelity measures. IEEE signal processing magazine **26**(1), 98–117 (2009) 29

75. Wu, Y., He, K.: Group normalization. In: Proceedings of the European conference on computer vision (ECCV). pp. 3–19 (2018) 36
76. Yen-Chen, L., Florence, P., Barron, J.T., Rodriguez, A., Isola, P., Lin, T.Y.: iNeRF: Inverting neural radiance fields for pose estimation. In: IEEE/RSJ International Conference on Intelligent Robots and Systems (IROS) (2021) 3, 5
77. Yu, A., Li, R., Tancik, M., Li, H., Ng, R., Kanazawa, A.: PlenOctrees for real-time rendering of neural radiance fields. arXiv preprint arXiv:2103.14024 (2021) 4
78. Yu, A., Ye, V., Tancik, M., Kanazawa, A.: pixelNeRF: Neural radiance fields from one or few images. In: Proceedings of the IEEE/CVF Conference on Computer Vision and Pattern Recognition. pp. 4578–4587 (2021) 2, 4, 11, 12, 13, 22, 29, 30, 31, 32
79. Zhang, R., Isola, P., Efros, A.A., Shechtman, E., Wang, O.: The unreasonable effectiveness of deep features as a perceptual metric. In: Proceedings of the IEEE Conference on Computer Vision and Pattern Recognition. pp. 586–595 (2018) 13, 29, 34
80. Zhang, W., Kosecka, J.: Image based localization in urban environments. In: Third international symposium on 3D data processing, visualization, and transmission (3DPVT'06). pp. 33–40. IEEE (2006) 5
81. Zhou, Q., Sattler, T., Pollefeys, M., Leal-Taixé, L.: To learn or not to learn: Visual localization from essential matrices. In: 2020 IEEE International Conference on Robotics and Automation (ICRA). pp. 3319–3326 (2020). https://doi.org/10.1109/ICRA40945.2020.9196607 5

ViewFormer: NeRF-free Neural Rendering
from Few Images Using Transformers

Supplementary material

In the supplementary material, we give more details on the results presented in the main paper and provide more details on the architecture. First, in Sec. A, we present additional qualitative results on various datasets. We also show the context views used to render the final view. The attached video is described in Sec. B. We include the camera pose estimation results on the 7-Scenes dataset [22] in Sec. C, and we also show qualitative results of the novel view synthesis task on the same dataset. In Sec. D we present an ablation study. We also show how the performance increases with larger context sizes. In Sections E and F we include additional results on the ShapeNet dataset and the Shepard-Metzler-Parts-7 (SM7) dataset. Quantitative results of the codebook model are given in Sec. G. Finally, we give details on the training hyperparameters and architecture of the models in Sections H and I.

A Qualitative results

We add qualitative results to the ones presented in the paper (see Fig. 1, 6, and 8 in the main paper). We show the context views together with the rendered images on the InteriorNet dataset [33] and on the Common Objects in 3D (CO3D) [54] dataset. The generated images are displayed in Fig. 9 and Fig. 10 respectively. We also show images generated with full context sizes in Fig. 11. It is important to note that all the visualizations, including the video, were rendered on previously unseen scenes (objects).

The images rendered on the largest and most complex dataset – InteriorNet, although being slightly blurry, resemble the ground truth (GT) images well. For the 7-Scenes dataset, the trained model overfitted the data, and therefore the quality of the generated images was not as good as on other datasets. Notice how the image rendered on CO3D is smoother than the ground truth image. In the case of the vase, we can see that the model could not represent the particular shape of the vase and used a simpler shape instead. This is an intriguing property of the model which in the case of incomplete information uses its large prior to achieve more realistic renderings at the cost of being less similar to the real object.

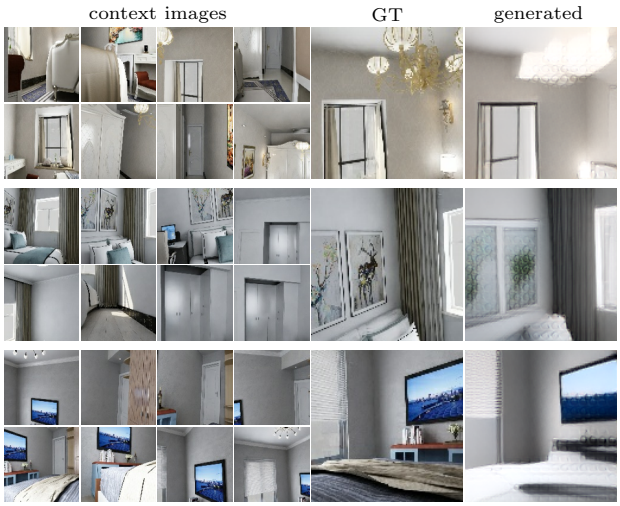

Fig. 9. Visualization of the model trained on the InteriorNet dataset [33]. We show the images generated with context size 8 while the model was trained with context size 19

B Attached video

We attach a video file[7] showing the generated images on various datasets. The video contains the results generated on the ShapeNet, CO3D, InteriorNet, and 7-Scenes datasets. On the ShapeNet dataset, we compare our model with PixelNeRF [78]. We render video sequences of rotating objects using three same context views. For the CO3D dataset, we show video sequences of rotating objects using 9 context views. We also show how the model changes its prediction given more context views. Unfortunately, we cannot compare with PixelNeRF [78] because the method was not able to converge properly on the dataset (see Sec. 4 in the main paper). Also, we cannot compare with NerFormer [54] because the source code is not publicly available. Finally, we show the results on the InteriorNet dataset as well as on all scenes from the 7-Scenes dataset.

From the sequences generated on the ShapeNet dataset, we can see that the rendered images are captured from correct poses, and the camera's motion is preserved. This implies that although the codes are discrete, they can represent a continuous motion of an object in the 3D space. It is interesting to see that our approach is occasionally not color consistent from frame to frame, *e.g.*, see the police car at time 0:07. We believe that the cause of this problem may stem from the codebook. It was trained using perceptual loss, which could be less sensitive to colors [19]. On the InteriorNet dataset (time 3:02), look at the pictures on the wall. The model first generates a window in place of the pictures, and with

[7] https://jkulhanek.github.io/viewformer/video

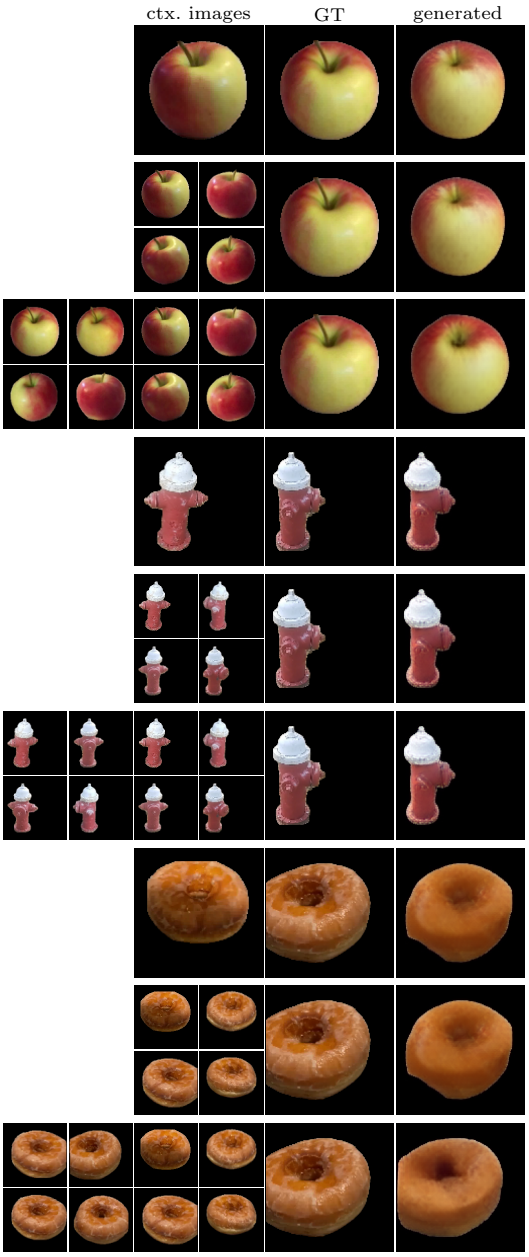

Fig. 10. Visualization of the model trained on the CO3D dataset [54]. We show the images generated with context sizes 1, 4, and 8 while the model was trained with context size 9

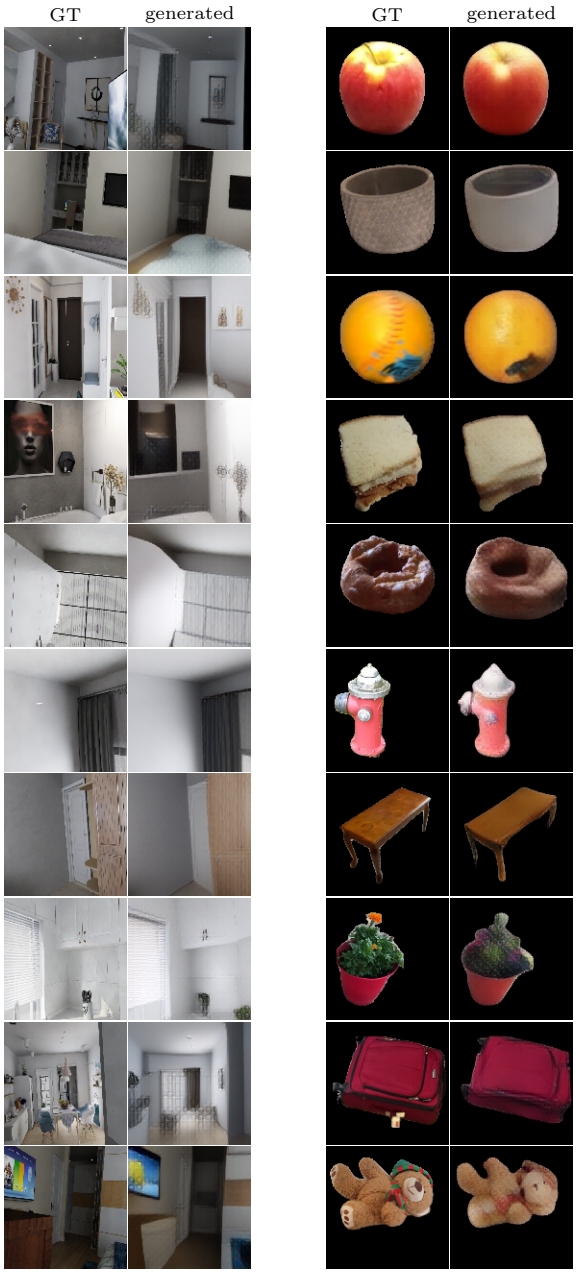

Fig. 11. Images generated on the InteriorNet dataset (**left**) with context size 19 and the CO3D dataset (**right**) with context size 9. For the CO3D evaluation, we used the model trained on all categories

more context views, it replaces the window with two pictures. This illustrates well how the model improves its prediction given more context views.

C 7-Scenes evaluation

Table 2. Camera pose estimation accuracy on the 7-Scenes dataset [22], reported as the mean median position (in meters) and orientation (in degrees) errors over all scenes. We report results with an InteriorNet pre-trained codebook ('-in') and a codebook fine-tuned on 7-Scenes ('-7s'). We further compare a simple decoding scheme (random context views) with a variant that uses the top-10 most similar training images for each query view ('top10'), identified via image retrieval

Method	All Pos/Ori	Chess Pos/Ori	Fire Pos/Ori	Heads Pos/Ori	Office Pos/Ori	Pumpkin Pos/Ori	Kitchen Pos/Ori	Stairs Pos/Ori
ViewFormer-in	0.24/10.49	0.16/8.03	0.24/11.35	0.17/13.23	0.25/10.33	0.23/8.20	0.31/11.01	0.30/11.28
ViewFormer-in-top10	0.19/7.82	0.13/6.36	0.22/10.27	0.17/10.85	0.17/6.42	0.19/6.26	0.21/6.62	0.21/7.97
ViewFormer-7s	0.23/8.46	0.15/6.31	0.23/10.03	0.19/12.68	0.23/7.69	0.19/5.59	0.27/7.75	0.31/9.18
ViewFormer-7s-top10	0.17/6.68	0.12/4.85	0.20/8.65	0.17/10.41	0.15/5.11	0.16/4.78	0.18/5.01	0.22/7.93
Oracle-top10	0.21/10.01	0.18/9.16	0.27/10.37	0.12/11.44	0.22/8.33	0.24/8.20	0.26/9.72	0.19/12.85
PoseNet [30]	0.44/10.4	0.32/8.12	0.47/14.4	0.29/12.0	0.48/7.68	0.47/8.42	0.59/8.64	0.47/13.8
MapNet [7]	0.18/6.56	0.09/3.24	0.20/9.29	0.12/8.45	0.19/5.45	0.19/3.96	0.20/4.94	0.27/10.57
LENS [43]	0.05/2.5	0.04/2.0	0.03/1.5	0.02/1.5	0.09/3.6	0.08/3.1	0.07/3.4	0.03/2.2
MS-Transformer [63]	0.18/7.28	0.11/4.66	0.24/9.6	0.14/12.19	0.17/5.66	0.18/4.44	0.17/5.94	0.26/8.45
RelocNet [1]	0.21/6.72	0.12/4.14	0.26/10.4	0.14/10.5	0.18/5.32	0.26/4.17	0.23/5.0	0.28/7.53
CamNet [18]	0.04/1.69	0.04/1.73	0.03/1.74	0.05/1.98	0.04/1.62	0.04/1.64	0.04/1.63	0.04/1.51
DenseVLAD [62, 70]	0.26/13.1	0.21/12.5	0.33/13.8	0.15/14.9	0.28/11.2	0.31/11.3	0.30/12.3	0.25/15.8
DenseVLAD+Int. [62]	0.24/11.7	0.18/10.0	0.33/12.4	0.14/14.3	0.25/10.1	0.26/9.42	0.27/11.1	0.24/14.7
DSAC* [6]	0.03/1.36	0.02/1.10	0.02/1.24	0.01/1.82	0.03/1.15	0.04/1.34	0.04/1.68	0.03/1.16
hloc [59]	0.03/1.09	0.02/0.85	0.02/0.94	0.01/0.75	0.03/0.92	0.05/1.30	0.04/1.40	0.05/1.47
Active Search [61]	0.04/1.18	0.03/0.87	0.02/1.01	0.01/0.82	0.04/1.15	0.07/1.69	0.05/1.72	0.04/1.01

In order to evaluate the performance of camera pose estimation, we present the results on the localization benchmark dataset – 7-Scenes [22] (*cf.* Sec. 4 in the main paper). We trained 2 models – one with a fine-tuned codebook and the other one with the InteriorNet-trained codebook. For all models we used context size 19. We have evaluated the method on all views from the test set of each of the 7 scenes and used the views from the training set as context images. Generated images can be seen in Fig. 12.

For localization, we have experimented with different strategies for obtaining the context view required by our approach: per default, we simply randomly select 19 training images as context for each test image. We further evaluate a variant that uses the top-10 most similar images identified via image retrieval with DenseVLAD [70] descriptors (indicated as "-top10"). The remaining 9 context images are randomly selected from the training images. We also experimented with using the top-19 retrieved images, but found this approach to work worse. We attribute this to the fact that the images of the 7-Scenes datasets are taken in sequences and that there is little viewpoint variation between the top-19 retrieved images.

We evaluate variants where the codebook is trained only on InteriorNet (indicated as "-in") and where the codebook is fine-tuned on the training images of

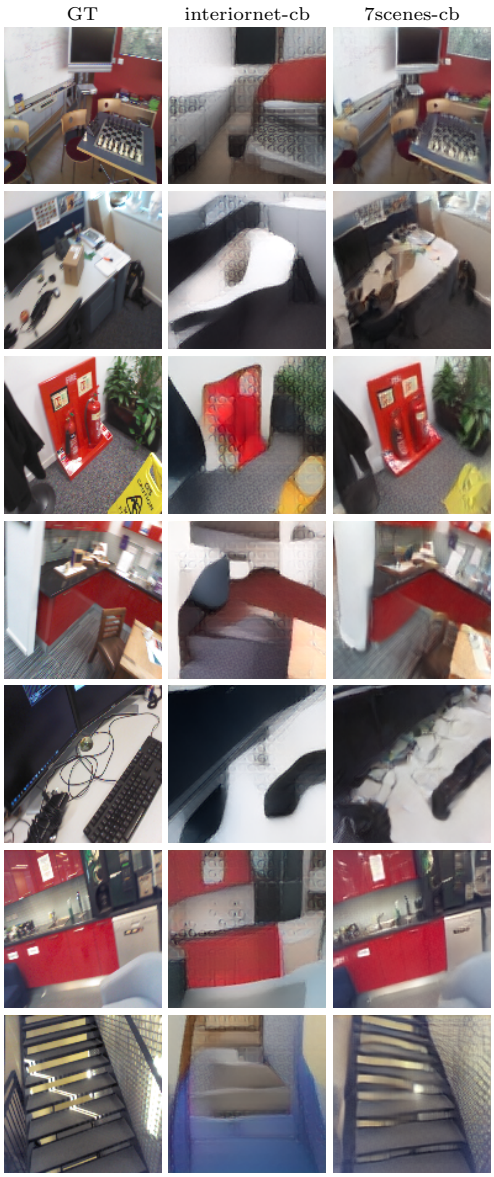

Fig. 12. Evaluation of the transformer model on the 7-Scenes dataset [22]. We display the ground-truth image (**GT**), the image generated using a codebook trained only on the InteriorNet dataset (**interiornet-cb**) and the image generated by a model with codebook fine-tuned on the 7-Scenes (**7scenes-cb**). For the visualization the context size was set to 19

7-Scenes ("-7s"). As can be seen in Tab. 2, using a fine-tuned codebook improves performance. Similarly, using the top-10 retrieved images leads to more accurate camera poses. For evaluation, we follow the common practice and report the median position and orientation error per scene, as well as the mean median position and mean median orientation error over all the scenes.

To better understand the performance of our approach, we compare it against an oracle. Given the top-10 retrieved images via DenseVLAD, the oracle selects the retrieved image with the smallest position and the smallest orientation error. As shown in Tab. 2, our approach outperforms the oracle on most scenes. This implies that the model is able to interpolate the context views such that it generates a pose which is closer to the query than any other in the context.

Tab. 2 also includes comparison with various baselines. Absolute pose regression techniques [7, 30, 43, 63] train a CNN to directly regress the camera pose for a given input image. Our approach performs similarly well or better than these baselines, with the exception of LENS [43], which uses additional training data in the form of images rendered from novel viewpoints. Our approach also typically outperforms the two image retrieval-based baselines (DenseVLAD and DenseVLAD + Int.) They were proposed in [62] as a form of sanity check for absolute pose regression approaches.

Similar to our approach, relative pose regression approaches [1, 18] estimate the pose of the test image *wrt.* a set of context views. These context views are obtained by finding the most similar training images using image retrieval. Our approach performs similarly well (and often better) as RelocNet [1], which also uses a single forward pass to regress relative poses (between pairs of images). CamNet uses a more complicated pipeline consisting of coarse and fine relative pose regression stages, which results in a higher accurary.

Structure-based approaches use 2D-3D matches between pixels in a test image and 3D scene points [5, 59, 61]. These approaches currently represent the state-of-the-art in terms of pose accuracy and are more accurate than pose regression-based techniques. In contrast to the other baselines, they store the 3D structure of the scene. Overall, the results show that our approach achieves a similar level of pose accuracy as comparable methods.

D Ablation study

We compare our model with alternative architectures to validate the design choices we made. We also demonstrate how the quality of predictions improves with larger context sizes. The InteriorNet dataset [33] was used for all evaluations because of its large size. The context size was 19.

Different model variants. We compare variants of our approach trained for only one of the two tasks – image generation and localization – on the InteriorNet dataset [33]. We evaluate our model trained only for localization or image generation. We also evaluate the importance of the proposed branching attention by training alternative models that do not use it. As discussed in Sec. 1 in the main paper, one way to train the transformer without the branching attention is

to have a purely autoregressive (causal) model [49, 72]. These models were successfully applied to similar tasks in prior work [21, 48, 51]. We also train another alternative – masked language models – that benefits from the same inference speed as our method [17]. In particular, the following models are compared:

- **ViewFormer** – our approach with both localization and image generation enabled.
- **ViewFormer no-loc** – our approach without localization.
- **ViewFormer no-imagen** – our approach without image generation.
- **Causal LM** – the same transformer model with autoregressive decoding. Instead of decoding all tokens at once, we model the probability distribution over next image token given all previous tokens [49, 72].
- **Causal LM + masked loc.** – causal LM with added localization. For the localization, we mask the poses of three random views from the training batch and attach a regression head to the last token of each image.
- **Masked LM** – the same transformer model with masked decoding (without the branching attention). We randomly mask three views from the training sequence and train the model to recover it. Note that the model is optimized for a single context size (previous variants optimized for all context sizes).
- **Masked LM + masked loc.** – masked LM with added localization. For the localization, we mask the poses of three random views from the training batch and attach a regression head to all image tokens. The resulting poses are averaged in the same way as in ViewFormer.

The results (averaged over all test scenes) are shown in Tab. 3. We also include a qualitative comparison in Fig. 13. As can be seen, training without the localization task improves image quality, whereas there is little difference in terms of pose accuracy between training with or without the generation. Therefore, there is likely enough capacity to capture both tasks in a single model.

Our method outperforms both causal LM and masked LM in image generation performance and localization accuracy. Note that our decoding is much faster compared to causal LM because we decode all tokens at once (see Section 1 in the main paper). For a causal LM, generating a single view takes 10 s even when using cache. Compare this to 93 ms for the ViewFormer. Compared to masked LM, our model has the same inference speed, but the added benefit of being optimized for all context sizes. Masked LM can be optimized for one context size only.

Increasing the context size. We show the effect of increasing the context size on the localization and image generation performance. The image generation performance (measured with PSNR) and the localization accuracy (median distance between the predicted camera position and the ground truth) are shown in Fig. 14. The results were computed on all scenes from the test set.

We can see that the performance of both novel view synthesis and camera pose estimation increases with more context views. The change is most prominent in the first five views, but after that it keeps increasing as well.

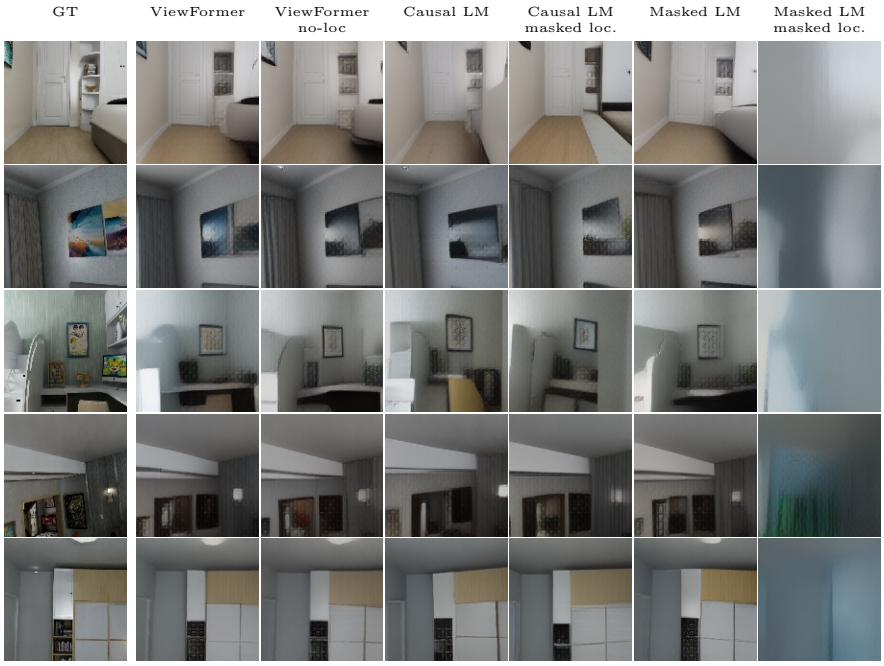

Fig. 13. Examples generated by alternative architectures described in Sec. D. The examples were generated on the test set of the InteriorNet dataset using context size 19.

Table 3. Ablation study evaluated on the InteriorNet dataset [33]. See Sec. D for a description of the compared variants. We show the PSNR, the pixel-wise MAE, and the LPIPS distance [79]. For localization, we show the median position error in meters and the median orientation error in degrees computed over all scenes.

	Image generation			**Localization**
Method	PSNR↑	MAE↓	LPIPS↓	Pos/Ori↓
ViewFormer	18.53	23.35	0.33	**0.19**/**4.22**
ViewFormer no-loc	**19.10**	**21.56**	**0.32**	-
ViewFormer no-imagen	-	-	-	**0.19**/4.34
Causal LM	16.75	29.88	0.39	-
Causal LM + masked loc.	16.67	30.22	0.39	0.22/6.24
Masked LM	18.76	22.91	**0.32**	-
Masked LM + masked loc.	14.51	42.89	0.51	0.32/29.65

E ShapeNet evaluation

In this section, we give more details on the ShapeNet results from the main paper (Fig. 7). We include quantitative and additional qualitative results. We trained our model on ShapeNet dataset rendered by SRN [67]. The context size used for training was three. We compare ViewFormer with SRN [67] and PixelNeRF [78]. We show the PSNR and SSIM [74] averaged across color channels for both car

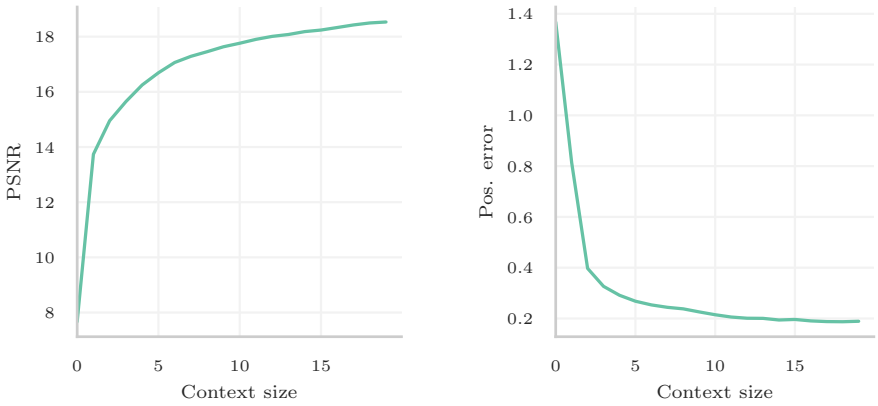

Fig. 14. This plot shows the effect of increasing the context size on the PSNR (**left**) and the position error (**right**) evaluated on the InteriorNet dataset [33]

Table 4. ShapeNet results comparing ViewFormer with SRN [67] and PixelNeRF [78]. We show the results for both car and chair category with one or two context views

		cars 1 view		cars 2 views		chairs 1 view		chairs 2 views	
Method	3D	PSNR↑	SSIM↑	PSNR↑	SSIM↑	PSNR↑	SSIM↑	PSNR↑	SSIM↑
ViewFormer	✗	19.03	0.83	20.09	0.85	14.74	0.79	17.20	0.84
SRN [67]	✓	22.25	0.89	24.84	0.92	22.89	0.89	24.48	0.92
PixelNeRF [78]	✓	23.72	0.91	26.20	0.94	23.17	0.90	25.66	0.94

and chair category with one or two context views. The results are presented in Tab. 4. We also extend the Fig. 7 from the paper by additional qualitative results on cars and chairs in Fig. 15 and 16.

From the results we can see that our method performs worse than both SRN [67] and PixelNeRF [78] in terms of the quantitative results. This is expected because our method was designed for more views (more than 10) and was evaluated using one or two views. However, compared to PixelNeRF our method is able to recover more detail, whereas PixelNeRF produces blurry output especially on the car category. Based on the qualitative results, we argue that although having worse quantitative numbers our results look more realistic. A possible cause for this observation could be that blurring the edges of an object can hide the unprecise geometry rendered by the model and increase PSNR. However, it loses fine detail in the images.

F Shepard-Metzler-Parts-7 evaluation

We evaluated our model on the Shepard-Metzler-Parts-7 dataset [20,64] to compare our approach to other methods that only operate in 2D [14,20,69]. For the

Fig. 15. Additional **ShapeNet** cars qualitative comparison with PixelNeRF [78] using two context views

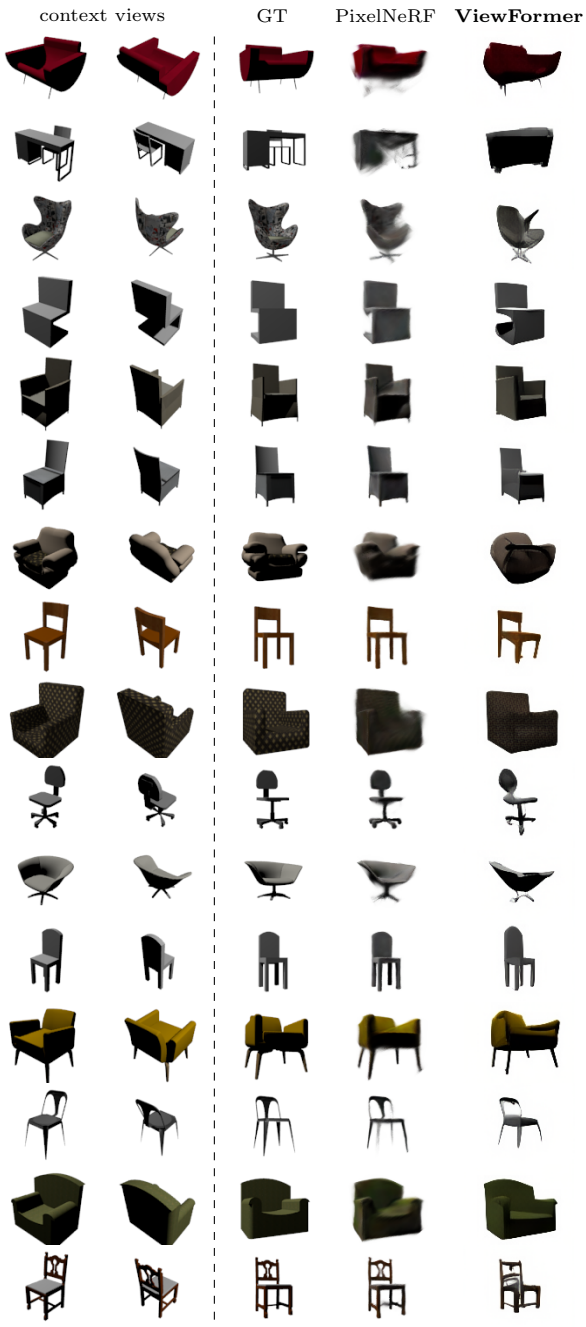

Fig. 16. Additional **ShapeNet** chairs qualitative comparison with PixelNeRF [78] using two context views

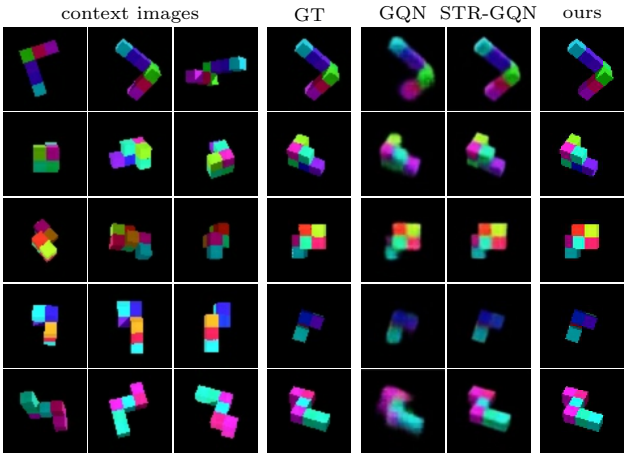

Fig. 17. Qualitative results on the SM7 dataset [20]. We compare against GQN [20] and STR-GQN [14]

Table 5. Comparison with GQN-based methods [13, 20, 69] on the SM7 dataset. We show the **MAE**, **RMSE**, and the position and orientation errors (**Pos**, **Ori**)

	Image generation		**Localization**
Method	MAE↓	RMSE↓	Pos/Ori↓
ViewFormer	**1.61**	7.02	0.21/3.48
GQN [20]	3.13	9.97	-
E-GQN [69]	2.14	**5.63**	-
STR-GQN [13]	3.11	10.56	-

evaluation, we used the context size three. The additional qualitative results, presented in Fig. 17, extend Fig. 5 from the main paper. Unfortunately, in the qualitative analysis, we cannot compare with E-GQN [69] because the authors did not make the generated images or models public.

Tab. 5 presents quantitative results (averaged over 1000 scenes). As our method uses images of sizes 128×128 pixels, we rescaled the images before training the codebook. For evaluation, we used the original image size 64×64 pixels of the dataset. We report the pixel-wise mean absolute error (MAE) and root mean square error (RMSE). For reference, we also show the localization accuracy. The position error (Pos) is the median distance between the predicted positions and the ground-truth camera positions, and the orientation error (Ori) is the median of the angular distances in degrees.

As can be seen, our method clearly outperforms the baselines in terms of the MAE. E-GQN performs best in terms of the RMSE as it is trained to optimize this metric, whereas our method uses MAE and the perceptual loss.

Table 6. Codebook evaluation on SM7 [20, 64], InteriorNet [33], CO3D [54], and 7-Scenes [22] datasets. We report the PSNR, MAE, and LPIPS metrics averaged over 1000 sampled images. The codebooks were evaluated with image size 128×128, except for 'CO3D@400', which was evaluated with image size 400×400 pixels

dataset	PSNR↑	MAE↓	LPIPS↓
SM7	36.96	1.06	0.0075
InteriorNet	24.86	11.01	0.1966
CO3D	25.14	5.70	0.0994
CO3D@400	25.34	5.63	0.1670
7-Scenes (fine-tuned)	19.29	17.51	0.2937
7-Scenes	19.00	19.22	0.3621
ShapeNet-cars	23.50	5.46	0.0734
ShapeNet-chairs	27.43	2.75	0.0425

G Codebook evaluation

In this section, we add more details on the codebook's representation capabilities (see Fig. 4 in the main paper) by showing the quantitative results. We evaluated the codebook models on each dataset's test set. We report the peak signal-to-noise ratio (PSNR), mean absolute error computed in the RGB image space (MAE), and the LPIPS distance [79]. All codebooks were evaluated with image size 128×128 pixels except for 'CO3D@400', which was evaluated with image size 400×400 pixels to be comparable with [54]. The metrics are averaged over 1000 randomly sampled images. The results can be seen in Tab. 6.

Before training the final codebook, we have experimented with different codebook models. We also trained the DALL·E codebook [51], which yielded slightly blurry images even when we used the codebook of size 8192 (normally, we use the codebook of size 1024). We observed a similar outcome with our codebook when we did not use the perceptual loss. We also tried to use the GAN loss for the codebook (as described in [21]), however, the generated images did not look geometrically consistent.

H Training details

To allow our results to be reproduced, we give the details on the architecture of our method as well as the training hyperparameters.

All our **codebook models** were trained using the same set of hyperparameters.[8] We trained codebooks of size 1024. The architecture is very similar to [21] and is summarized in Sec. I. We used the Adam optimizer [31] with learning rate[9] 1.584×10^{-3} to train for 200k steps (roughly 480 GPU-hours) with a batch size of 352. For the CO3D dataset, we trained on the same 10 object categories

[8] Except for the SM7 dataset where we only fine-tuned an existing model.
[9] The learning rate was rescaled from prior experiments; 1.6×10^{-3} would work too.

as in [54] as well as on the full dataset. For the 7-Scenes dataset, due to not having enough images, we finetuned an InteriorNet pre-trained model. Therefore, we used only 20k batch updates with the same hyperparameters.

The architecture of our **transformer model** is based on GPT2-base, [49] and has 12 transformer blocks, 12 attention heads, and the hidden size is 768. The model design was chosen based on its successes in other domains and because its size fits well on our hardware. We trained our transformer models using the AdamW optimizer [38]; we used the cosine schedule for the learning rate with 2k step linear warmup.

For the **InteriorNet dataset**, we used the mixed precision training with learning rate 8×10^{-5}, batch size 40, and learning rate decay 0.01. The context size was 19, but we did not optimize the first four views. The weight of the localization loss term was 5. In all other experiments the localization loss weight was 1 unless stated otherwise.

For the **Shepard-Metzler-7-Parts (SM7)** [20, 64] dataset, we trained the transformer for 120k steps with the context size 5, batch size 128, and the learning rate 10^{-4} (cosine decay, warmup). Before passing camera poses into the transformer, we normalized the positions by multiplying them by 0.2. We also gradually increased the weight of the localization term from 0 to 1 using the cosine schedule.[10]

For the **CO3D dataset**, we fine-tuned the model trained on the InteriorNet dataset. For the 10 categories, we optimized the model for 40k gradient steps with learning rate 10^{-4} (cosine decayed with 2000 step warmup), weight decay 0.05, and batch size 80, employing mixed precision training. The context size was 9, and the batch size was 80. We scaled the camera positions by 0.05 in order for the positions to have a similar range as the pre-trained model. We also trained a model on all dataset categories using 100k gradient steps with the batch size 40, without using mixed precision training, and when using the localization, we further used gradient clipping with the norm 1 to improve stability.

For the **7-Scenes dataset**, we used a single InteriorNet pre-trained model which we fine-tuned on all 7-Scenes scenes. Same as in the original model, the context size was 19, but we did not optimize the first four views. The transformer was fine-tuned for 10k gradient steps with learning rate 10^{-5} (cosine schedule, warmup). We multiplied the positions by 5 to be consistent with InteriorNet.

Finally, for the **ShapeNet dataset**, we fine-tuned InteriorNet pre-trained model as well. We trained a single model for both categories: cars and chairs with the context size 3. We did not use mixed precision training and batch size was 64. The transformer was fine-tuned for 100k gradient steps with learning rate 10^{-4} (cosine schedule, warmup), weight decay was 0.05, and we used gradient clipping with the norm 1.

[10] The schedule is not needed for the training to work and in newer experiments we use a constant instead.

Table 7. Codebook architecture details: the encoder (**top left**), the decoder (**right**), and the residual block (**bottom left**). For each layer, we list the number of output features (Num. features) and the size of the output features (Out. size). We denote kernel size as 'ks', stride as 's', and number of groups as 'g'. We use nearest neighbor for the Upsample 2D layer. Note that the output of the residual block is added to its input as in ResNets [23]. If the number of input channels is not equal to the number of output channels, the residual connection is implemented by applying an affine transformation to input features position-wise before summing them with the output of this block

Layer type	Num. features	Out. size
Conv 2D (ks: 3)	128	128
ResBlock	128	128
ResBlock	128	128
Conv 2D (ks: 3, s: 2)	128	64
ResBlock	128	64
ResBlock	128	64
Conv 2D (ks: 3, s: 2)	128	32
ResBlock	256	32
ResBlock	256	32
Conv 2D (ks: 3, s: 2)	256	16
ResBlock	256	16
Attention 2D	256	16
ResBlock	256	16
Attention 2D	256	16
Conv 2D (ks: 3, s: 2)	256	8
ResBlock	512	8
ResBlock	512	8
ResBlock	512	8
Attention 2D	512	8
ResBlock	512	8
GroupNorm 2D [75] (g: 32)	512	8
Swish [50]	512	8
Conv 2D (ks: 3)	256	8
Conv 2D (ks: 1)	256	8

(a) Encoder

Layer	Num. features
GroupNorm [75] (g: 32)	in
Swish [50]	in
Conv 2D (ks: 3)	out
GroupNorm [75] (g: 32)	out
Swish [50]	out
Conv 2D (ks: 3)	out

(b) ResBlock

Layer type	Num. features	Out. size
Conv 2D (ks: 1)	256	8
Conv 2D (ks: 3)	512	8
ResBlock	512	8
Attention 2D	512	8
ResBlock	512	8
ResBlock	512	8
ResBlock	512	8
ResBlock	512	8
Upsample 2D	512	16
Conv 2D (ks: 3)	512	16
ResBlock	256	16
Attention 2D	256	16
ResBlock	256	16
Attention 2D	256	16
ResBlock	256	16
Attention 2D	256	16
Upsample 2D	256	32
Conv 2D (ks: 3)	256	32
ResBlock	256	32
ResBlock	256	32
ResBlock	256	32
Upsample 2D	256	64
Conv 2D (ks: 3)	256	64
ResBlock	128	64
ResBlock	128	64
ResBlock	128	64
Upsample 2D	128	128
Conv 2D (ks: 3)	128	128
ResBlock	128	128
ResBlock	128	128
ResBlock	128	128
GroupNorm 2D [75] (g: 32)	128	128
Swish [50]	128	128
Conv 2D (ks: 3)	128	3

(c) Decoder

I Codebook architecture

In Tab. 7 we give the details on the codebook architecture (*cf.* Sec. 3 in the main paper). The codebook model architecture was taken from [21] and modified slightly to downscale the images into a two times smaller latent space. We had chosen this architecture because it had showed promising results for image generation in combination with transformers [21]. The other architecture we had considered was DALL·E [51], but from our experiments it performed worse.